

Electric-field control of zero-dimensional topological states in ultranarrow germanene nanoribbons

Lumen Eek^{1#}, Esra D. van 't Westende^{2#}, Dennis J. Klaassen², Harold J. W. Zandvliet², Pantelis Bampoulis^{2*}, and Cristiane Morais Smith^{1*}

¹*Institute for Theoretical Physics, Utrecht University, Princetonplein 5, Utrecht, 3584 CC, the Netherlands.*

²*Physics of Interfaces and Nanomaterials, MESA+ Institute for Nanotechnology, University of Twente, Drienerlolaan 5, Enschede, 7522 NB, the Netherlands.*

shared first authors

* corresponding authors:

p.bampoulis@utwente.nl

c.demoraissmith@uu.nl

Date: May 2 2025

Symmetry-protected zero-dimensional (0D) modes, such as corner and end states with fractionalized charge, promise robust qubits and efficient electronics. Yet, reversible, electric-field manipulation and control of these modes has remained elusive. Here, we show theoretically and experimentally electric-field-driven on/off switching of 0D topological end modes in two- and three-hexagon wide germanene nanoribbons in a vertical tunnel junction set-up. We demonstrate the annihilation and restoration of end states in topological samples, but also the induction of 0D topological modes in initially trivial ribbons. The process is reversible, and the system operates at 77 Kelvin. This atomic-scale platform realizes a proof-of-principle for a 0D topological field-effect device, opening an unexpected path for ultra-small memory, quantum computing, and neuromorphic architectures.

Topological insulators (TIs) have transformed condensed-matter physics by revealing the existence of symmetry-protected boundary states that are beyond conventional band-theory descriptions [1–4]. In particular, zero-dimensional (0D) modes have attracted much attention because of their potential use as qubits in quantum computers [5]. Experimentally, 0D states have been observed as corner modes in higher-order TIs [6,7] and localized states in topological superconductors [8–11]. In 1D honeycomb systems, 0D topological states have emerged as transition states in graphene nanoribbons [12] or 0D end states in ultranarrow graphene [12–14] and germanene nanoribbons [15]. However, their utility and further investigation hinges on controlled and reversible manipulation of their topological state using an external stimulus, ideally using an electric field compatible with nanoscale gating [16–21]. Although electric-field switching has been demonstrated in 2D TIs (e.g. germanene, Na₃Bi) [17,18], it remains unrealized for 0D modes.

In this work, we demonstrate reversible, electric-field–induced switching of 0D end modes in epitaxially grown germanene nanoribbons. Germanene, a low-buckled honeycomb monolayer of Ge atoms [18, 20, 22], belongs to the material family of 2D Xenes with novel electronic properties [23–25]. Germanene hosts a spin-orbit coupling induced gap at the K/K' points of the Brillouin zone and, in its 2D form, it is a Kane–Mele-type TI (class AII) with helical edge states [18,26]. When narrowed to about 1 nm, germanene nanoribbons undergo a transition into a 1D TI with in-gap end modes protected by time-reversal and mirror symmetries, which carries fractionalized charge [15]. Using tight-binding calculations and 77 K scanning tunneling microscopy and spectroscopy (STM, STS), we show that a perpendicular electric field in a vertical tunnel-junction architecture can switch these 0D modes on and off. Particularly, it is possible to create and annihilate 0D end states in initially trivial ribbons, as well as to destroy and fully restore them in intrinsically topological ribbons. This smallest-possible (one atom thick and about 1 nm narrow) platform demonstrates a proof-of-principle 0D topological field-effect device and paves the way for switchable, energy-efficient quantum electronics based on symmetry-protected states. We envisage that this field-driven mechanism will enable ultra-small building blocks for memory devices, quantum computing architectures, and neuromorphic computing platforms.

Ultrathin, zigzag-terminated germanene nanoribbons were grown via segregation-based epitaxy on Pt/Ge(110) (see Ref. [15] and Methods). Fig. 1a shows an STM overview image of an array of nanoribbons, aligned along [-110] and spanning various widths. A high resolution STM image of a two-hexagon-wide nanoribbon is shown in Fig. 1b. Its atomic-scale lattice is revealed in Fig. 1c, where the overlaid tentative ball-and-stick model [15] depicts a low-buckled honeycomb geometry. From the line profiles in Fig. 1d and Fig. 1e (taken respectively along the white and teal traces in Fig. 1b), we extract a lattice constant of about 4.2 Å and a buckling amplitude in the range of 0.2 Å to 0.3 Å for this ultranarrow nanoribbon. This low-buckled honeycomb germanene lattice is expected to interact weakly with the rectangular Pt/Ge(110) substrate due to the different lattice symmetries [15]. Along the long-axis ([-110] substrate direction), the ribbons terminate in zigzag edges.

Ribbons wider than six hexagons realize a 2D TI with helical 1D edge states [15]. A phase transition from a topological 1D edge state to a 0D end state was recently shown to occur for germanene nanoribbons thinner than about 2 nm [15]. In addition, it was theoretically demonstrated that the existence of topological end modes depends on a complex interplay of several parameters, such as the precise width of the nanoribbon, the intensity of the intrinsic spin-orbit coupling of the material, the value of the staggered Semenoff mass for Kane-Mele type systems, as well as the nearest neighbor, next-nearest neighbor, and next-next-nearest neighbor hopping parameters of the tight-binding model. Nevertheless, the end states, protected by a quantized Zak phase, were proven to exist in a broad regime of parameters, to be experimentally accessible with state-of-the-art microscopy, and to be robust [15]. Fig. 1f shows the STM topography (left panel) of a wide ribbon alongside its differential conductance (dI/dV) map (right panel), which clearly shows the 1D edge channels (pink) running continuously around the edges. In contrast, Fig. 1g shows the topography (left) and dI/dV map (right) of a nanoribbon with a width of two hexagons (about 1 nm). The end modes are shown in the corresponding dI/dV map (pink). Note that in STM, the

dl/dV signal is proportional to the local density of states (LDOS) and the topography image also contains a contribution of it

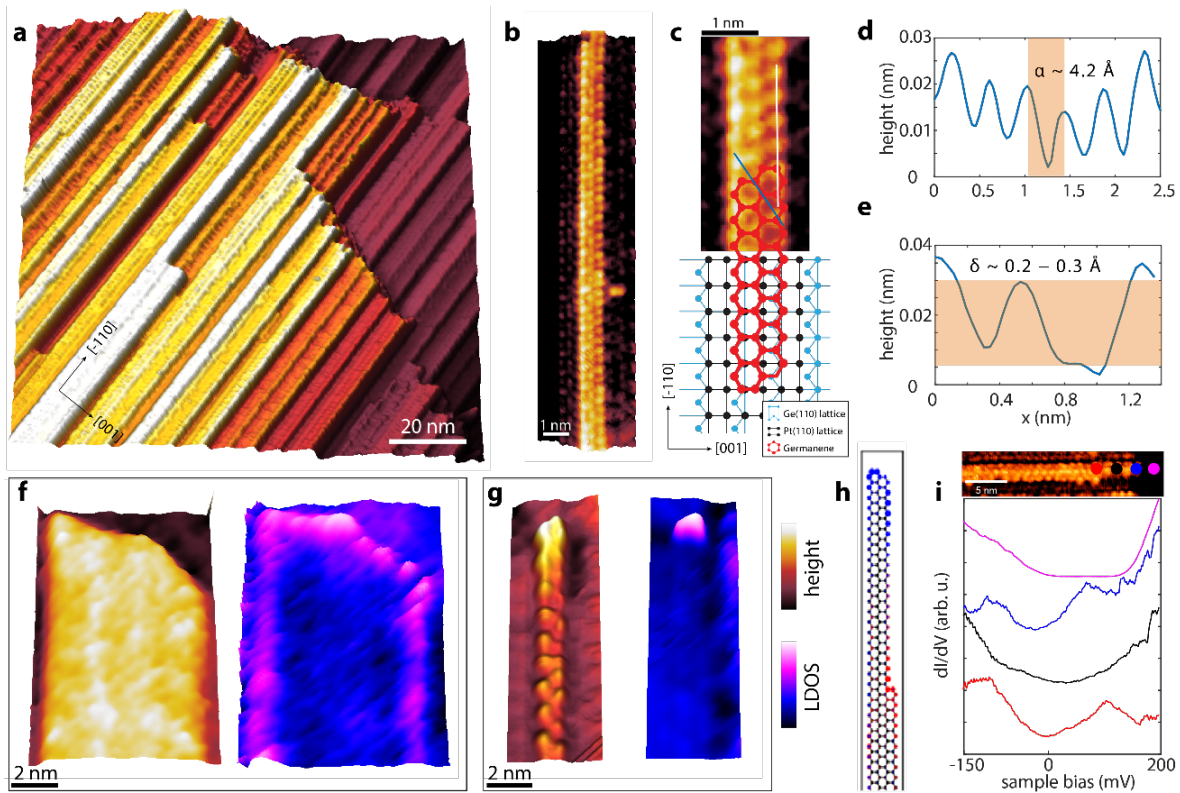


Figure 1. Atomic structure of the germanene nanoribbons. **a**, Large-scale STM topography showing an array of germanene nanoribbons of various widths running along the $[-110]$ substrate direction. **b**, Atomic-scale STM image showing a two-hexagon wide nanoribbon. **c**, (top) Atomic resolution of a two-hexagon wide nanoribbons overlaid with the tentative structural model. **d**, Line profile taken at the white line in **c** (along the nanoribbon). **e**, Line profile taken at the teal line in **c**, showing the buckling in the hexagonal lattice. **f**, Topography and dI/dV map (taken at 150 mV, 0.2 nA) of a wide nanoribbon. The dI/dV map reveals the edge state (pink). **g**, Topography and dI/dV map (taken at 50 mV, 0.2 nA) of a two-hexagon wide nanoribbon. The dI/dV map demonstrates the localization of the end state (pink). **h**, Topological states (red and blue) calculated theoretically for a nanoribbon with variable width, changing from two to three-hexagon wide. A pinned state is visible at the kink, in addition to the topological state at the end of the two-hexagon wide part. The red state hybridized and is visible on both the end and the kink. **i**, Topography (top) and $dI(V)/dV$ traces (bottom) measured experimentally, at the end of the nanoribbon (two-hexagon wide end), the middle of the nanoribbon, and the cross-over point from three- to two-hexagon wide. The locations where the traces were recorded are marked in the topography image.

The topological phase diagram of ultranarrow germanene ribbons exhibits a reentrant behavior with their width [14,15]. Therefore, it would be interesting to investigate a nanoribbon with a

domain wall, which realizes the critical three- to two-hexagon boundary defect, see Fig. 1h. Such nanoribbons are found scarcely in our samples, but an example is shown in Fig. 1i. The main theoretical and experimental results are shown in Figs. 1h and 1i, respectively. In addition to an end mode in the two-hexagon part of the sample (blue), there is a mode pinned at the interface between the two- and three-hexagon wide parts (red), see Figs. 1h and 1i. Moreover, the topological state at the two-three interface hybridizes strongly with the end state because the model system used for the calculations is not long enough, and the bulk gap of this ultranarrow sample is relatively small. Therefore, the topological end mode (blue) appears to be more prominent because it contains also a contribution from the mode at the two-three interface. Topological states at domain walls have been also realized in graphene nanoribbons [12,27], and represent a route towards band engineering in 1D systems.

The existence of robust 0D end modes in an intrinsic low-buckled honeycomb geometry makes ultranarrow germanene ribbons an ideal platform to explore electric-field-driven topological switching. The out-of-plane buckling separates the inverted π -orbitals onto distinct sublattices, which is crucial for field-induced phase transitions by breaking the band inversion symmetry. We examined the effect of a perpendicular electric field on the electronic structure of these ultranarrow germanene nanoribbons, and particularly on the end states. This was achieved by leveraging the built-in electric field in the STM tip-sample tunnel junction. The work function difference between the STM tip ($\text{PtIr} \sim 5.5$ eV) and germanene (~ 4 eV [61]) creates an electrostatic potential difference. The strength of this electric field depends not only on the difference in the work functions but also on the tip-sample separation, which can be precisely controlled via the tunneling current set-point [17,18]. This accurate control allows adjustments to the electric field relative to the initial tip-induced field. Because our sample voltage bias is small in comparison to the electrostatic potential difference, it can be neglected [18]. By adjusting the current setpoint in the tunnel junction, we can precisely modify the tip-sample distance relative to the reference (original) distance. A higher current setpoint corresponds to a smaller separation distance, leading to a stronger tip-induced electric field. Although any estimate of the absolute electric field magnitude will unavoidably include large systematic errors, mainly due to uncertainties in determining tip-sample distance, work functions, image charges, and tip-induced band bending [17,18], these produce only an overall offset. Crucially, the relative change in field is determined exactly by the current set-point. Therefore, we report all field-dependence in terms of the precisely known set-point currents rather than absolute field values. Low current setpoints (in the order of 0.2 nA) correspond to low electric fields, and high current setpoints (in the range of 2nA) correspond to higher fields.

Figure 2 shows the differential conductance $dI(V)/dV$ spectra measured at the bulk and end of a two-hexagon wide germanene nanoribbon for varying current setpoints. Figures 2a and 2b present, respectively, a sketch of the nanoribbon and its topographic image. Figure 2c shows the dI/dV as a function of voltage and distance from the endpoint of the ribbon. The variation in behavior as a function of electric field is presented in Figs. 2d-g and the influence of the electric field on a trivial surface state is shown in the Supplementary Information (SI). The differential conductance of the bulk (Fig. 2d) indicates that upon increasing the current setpoint (and thus the electric field), the gap narrows and eventually closes at a current $I = 2.2$ nA (see also dashed

black lines for a reference). Beyond this point, as the current setpoint increases further, the gap reopens, but it is then a trivial gap. This is confirmed by the measurements of the $dI(V)/dV$ at the end of the nanoribbon presented in Fig. 2e, which shows that the zero mode vanishes for values of current setpoint larger than 2.2 nA.

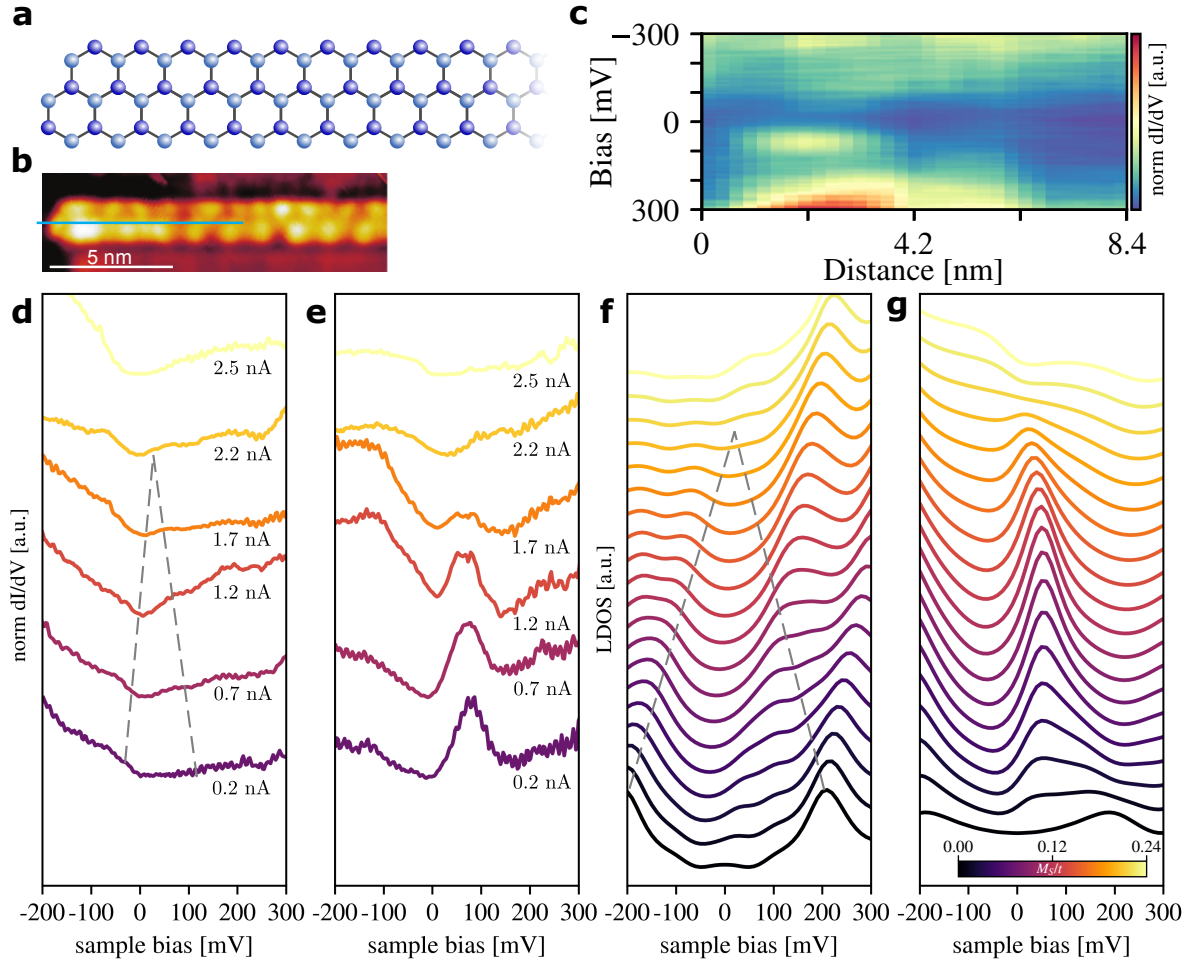


Figure 2: Electric field control of zero-dimensional topological end states in ultranarrow (2-hexagon wide) germanene nanoribbon. **a**, Sketch of the lattice structure. **b**, Atomic resolution measurement of the nanoribbon topography. **c**, dI/dV spectra as a function of bias voltage and real space distance, showing the localization of the state at the end of the ultrathin nanoribbon in **b**. **d,e**, Normalized $dI(V)/dV$ versus V measurements upon increasing the electric current that generates the electric field from $I = 0.2$ nA to $I = 2.5$ nA, for the bulk (**d**) and edge (**e**) of the sample. **f,g**, Theoretically calculated LDOS, for several values of the staggered mass M (see inset in **g** for the color code). The results for the bulk are shown in **f** and for the edge in **g**. The plots obtained for the lowest values of staggered mass (black curves in **g**) should not be compared to the experiments because the germanene samples always have a finite mass due to the buckling of the structure. The dashed lines in **d** and **f** indicate the closing of the bulk gap. In the corresponding

regime of parameters, a (slightly displaced) zero-bias peak may be observed at the edges, see **e** and **g**.

These results are corroborated by theoretical calculations using a tight-binding description based on the Kane-Mele model for graphene, see Fig. 2**f** for the bulk LDOS and Fig. 2**g** for the end. In addition, longer-range hopping must be taken into account because first-principles calculations have indicated that the next-next-nearest neighbor hopping parameter is sizable, and even larger than the next-nearest neighbor one [15,29,30]. The main difference with graphene is that germanene has a large intrinsic spin-orbit coupling (with a spin-orbit gap estimated to be of the order of 100 meV when germanene is in proximity to Pt [18]) and a staggered mass $M = 10 - 50$ meV, which must be included because of the inherently buckled structure of germanene. This also implies that the lowest plots of the LDOS for nearly vanishing staggered mass (black lines in Figs. 2**f** and 2**g**) should not be compared to the experiments because this mass is never zero. We nevertheless included them for completeness. The agreement between theory and experiments is remarkable.

Next, we show that the electric field is not only able to drive a topological to trivial transition in germanene nanoribbons, but also the opposite, namely, to induce topological phases in originally trivial ribbons. In Fig. 3, we compare the behavior of a two-hexagon and a three-hexagon wide nanoribbon. The regime of parameters for the realization of topological end-states in a two-hexagon wide nanoribbon is larger than for the three-hexagon wide case because the two-hexagon wide nanoribbon is topological for small electric fields, whereas the three-hexagon wide one is trivial, see Figs. 3**a** and 3**b**, respectively. Indeed, for small currents a peak corresponding to the topological end mode appears in the dI/dV of the two-hexagon wide ribbon (Fig. 3**c**), but not for the three-hexagon one (Fig. 3**d**). However, topology may not only be destroyed in the topological sample upon increasing the electric field to $I = 2.5$ nA (see Fig. 3**c**), but it may also be *induced in the trivial sample*, see Fig. 3**d**, where a peak emerges at higher values of the electric field ($I = 1.8$ nA setpoint current). These observations align well with the tight-binding calculations shown in Figs. 3**e** and 3**f** for the two- and three-hexagon wide nanoribbons, respectively, which predict an electric field-induced topological to trivial phase transition, as well as the opposite, from trivial to topological, depending on the width of the nanoribbon and on the model parameters. The parameters used here are shown as purple and orange dots in the phase diagrams in Figs. 3**a** and 3**b**, respectively.

This behavior can be understood by recalling that the electric field breaks inversion symmetry and induces a staggered sublattice potential (a tunable Semenoff mass), which through a complex interplay with the intrinsic spin-orbit coupling, leads to a rich phase diagram, with multiple topological and trivial regions (see SI and Refs. [26, 28]). For the two-hexagon wide ribbon, the initially topological hybridization gap closes in a continuous way at a critical electric field. Upon further increasing the field, the gap reopens with a trivial Zak phase, and the 0D end modes are no longer present. We have confirmed this bulk-end correspondence via the comparison between the closure/reopening of the gap with both, the calculated Zak phase and the STM spectra. On the other hand, the three-hexagon wide ribbon has originally a small trivial gap, which closes and reopens with a non-trivial Zak phase upon increasing the electric field.

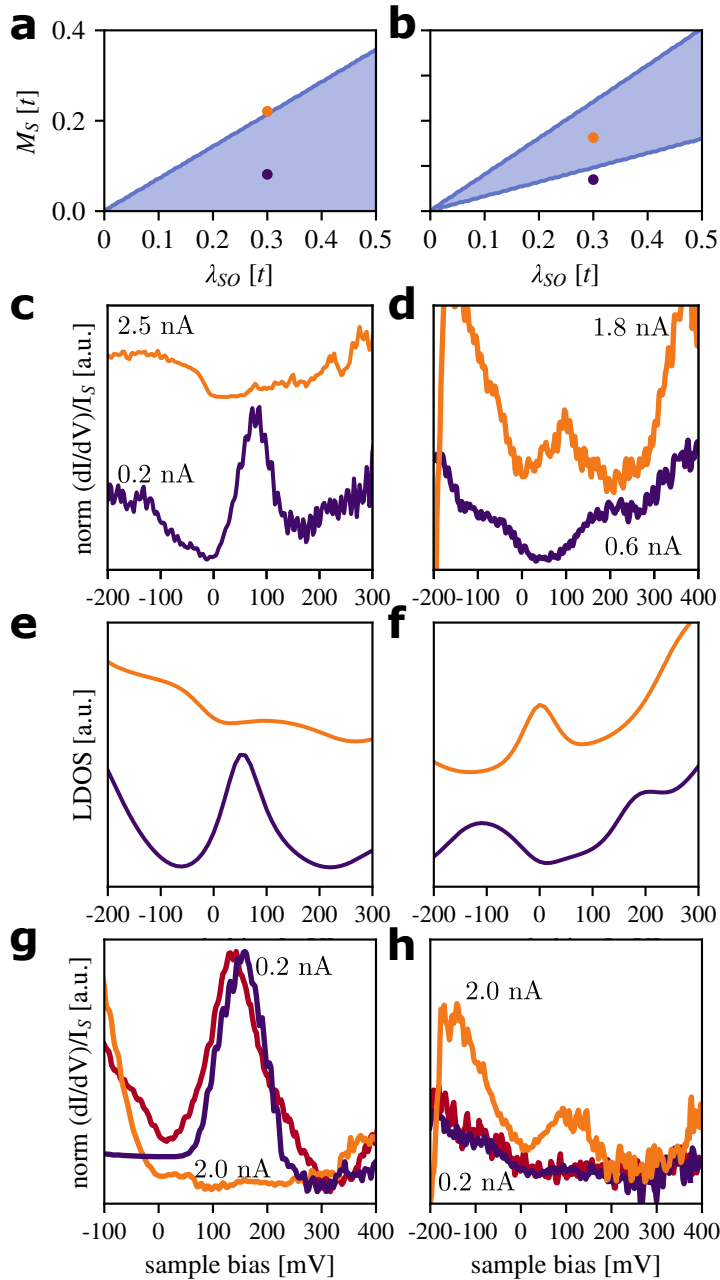


Figure 3: Comparison between 2-hexagon and 3-hexagon wide nanoribbons. **a,b**, Topological phase diagrams calculated for different values of the staggered mass M_S and intrinsic spin-orbit coupling λ_{SO} for the two- and three-hexagon wide nanoribbons, respectively. The topological regime is depicted in blue and the trivial regime in white. Notice the smaller parameter space for the existence of topological end states in the three-hexagon wide case. **c,d**, Experimentally detected dI/dV for two-hexagon (**c**) and three-hexagon (**d**) wide nanoribbons. For small electric fields, i.e. current setpoint $I \sim 0.2\text{ nA}$, the two-hexagon nanoribbon is topological and exhibits a pronounced peak at $V \sim 100\text{ mV}$ (purple curve in **c** and purple dot in **a**). Upon increasing the electric field, the peak reduces in intensity, until a trivial regime is reached at $I \sim 2.5\text{ nA}$, at which the topological end mode vanishes (orange curve). **d**, The three-hexagon wide nanoribbon

displays a trivial gap at $I \sim 0.6\text{ nA}$ (purple curve) but becomes topological at larger electrical fields. Indeed, a peak becomes visible at $I \sim 1.8\text{ nA}$ setpoint current, with maximal intensity around 100 mV (orange curve). **e,f**, Theoretical calculations for the two- and three-hexagon wide nanoribbons, confirming the experimental observations. The same color code is used for the curves. **g,h**, Reversible manipulation of the topological/trivial states with an electric field for the two- and three-hexagon wide nanoribbons, respectively.

Finally, we emphasize that this electric-field driven switching of the end states is *reversible*. In Fig. 3g, we provide current-setpoint sweeps for a two-hexagon wide nanoribbon, where increasing the current setpoint drives the ribbon from the topological into the trivial regime, removing the OD end states, and decreasing the setpoint back restores the low-field condition and the end modes re-emerge. Although the precise on/off thresholds and the amplitude of the recovered state vary from ribbon to ribbon and from cycle to cycle, probably due to slight tip changes or intrinsic hysteresis in the phase boundary, the underlying electric field control is clearly visible. Moreover, in Fig. 3h we show that the same reversible process occurs for the three-hexagon wide case.

The reversible electric-field switching of OD end modes in ultranarrow (about 1 nm wide) and ultrathin (one-atom thick) germanene nanoribbons presented here provides the first proof-of-principle for the realization of a OD topological field-effect device. Using the local gate formed by the STM tunnel junction, we achieve continuous closing and reopening of the bulk gap via controllable inversion-symmetry breaking, while tracking the emergence and vanishing of the end states. The experimentally achievable critical field (found to occur for setpoint currents in the range of 2 nA and estimated to be around 2-2.5 V/nm) and the small hysteresis confirm the robustness and reversibility of this mechanism. This atomic-scale platform not only validates the concept of a topological switch at the smallest conceivable device footprint, but also opens immediate pathways toward ultra-small low-energy memory cells, symmetry-protected qubits, and neuromorphic elements in future quantum-electronic circuits.

Methods

1. Experimental methods

1a. Scanning tunneling microscopy

STM data were acquired using a UHV Omicron low-temperature STM operating at 77 K. Samples were transferred from the preparation chamber, where they were grown, to the STM chamber under ultra-high vacuum conditions. The conductivity and sharpness of the tips were verified on either an Au or Pt-coated HOPG sample. Constant current STM imaging was performed with current setpoints typically ranging from 0.2 to 2.5 nA and voltage biases typically between -0.5 V to 0.5 V . The $dI(V)/dV$ spectra for STS were recorded with the feedback loop disabled, employing a lock-in amplifier with an AC modulation voltage of 10–20 mV at a frequency range of 1000–1200 Hz. Data processing and analysis of STM images and $dI(V)/dV$ spectra were carried out using MATLAB, Gwyddion, and SPIP.

1b. Nanoribbon growth

Germanene nanoribbons were grown on Ge(110) in ultra-high vacuum (base pressure in low 10^{-10} mbar) by first cleaning Ge(110) wafers via Ar^+ sputtering and high-temperature annealing (1150 K), then depositing about 1 ML of Pt and then flash annealing to 1150 K. Upon cooling down to room temperature, Ge atoms segregate on the Pt layer, forming extended, flat germanene ribbons when the underlying Pt coverage is near a full monolayer [15]. Lower local Pt coverage instead yields Ge nanowires [15]. Both ribbons and wires align along $[-110]$ due to the substrate symmetry, but only the ribbons reach lengths of hundreds of nanometers with atomically uniform honeycomb structure, such as the ones in Fig. 1.

1b. Tip-induced band bending

For materials significantly affected by tip-induced band bending (TIBB), increasing the current setpoint (or decreasing the tip-sample distance) would enhance band bending, resulting in a larger apparent gap. However, this behavior is inconsistent with our observations, where the gap decreases with increasing current setpoint. While the influence of TIBB cannot be entirely excluded at high current setpoints, it should lead to an increase of the bandgap, rather than a closing and reopening. Therefore, the size of the bandgap might be slightly overestimated because of this effect.

2. Theoretical Methods

2a. Hamiltonian

Germanene is composed of a monolayer of germanium atoms arranged in a buckled honeycomb structure. Consequently, its behavior around the Fermi level is well described by the Kane-Mele Hamiltonian,

$$H = t \sum_{\langle ij \rangle} \mathbf{c}_i^\dagger \mathbf{c}_j + t_2 \sum_{\langle\langle ij \rangle\rangle} \mathbf{c}_i^\dagger \mathbf{c}_j + t_3 \sum_{\langle\langle\langle ij \rangle\rangle\rangle} \mathbf{c}_i^\dagger \mathbf{c}_j + \frac{i\lambda_{SO}}{3\sqrt{3}} \sum_{\langle\langle ij \rangle\rangle} v_{ij} \mathbf{c}_i^\dagger s_z \mathbf{c}_j + i\lambda_R \sum_{\langle ij \rangle} \mathbf{c}_i^\dagger (\mathbf{s} \times \mathbf{d}_{ij})_z \mathbf{c}_j + M_S \sum_i \eta_i \mathbf{c}_i^\dagger \mathbf{c}_i, \quad (1)$$

where $\mathbf{c}_i = (c_{i,\uparrow}, c_{i,\downarrow})^T$ is a vector composed of electronic annihilation operators, t is the nearest-neighbor hopping parameter, λ_{SO} is the spin-orbit coupling, λ_R is the Rashba spin-orbit coupling and M_S is the staggered (Semenoff) mass. Additionally, v_{ij} is +1 (−1) for (counter) clockwise hopping and η_i is a staggering parameter which is either +1 or −1, depending on the sublattice. Furthermore $\mathbf{s} = (s_x, s_y, s_z)$ are the Pauli matrices acting on spin space and \mathbf{d}_{ij} is the vector connecting sites i and j . Additionally, longer range hopping terms, t_2 and t_3 , have been included, because first principle-calculations indicate that they are sizable in germanene.

In the absence of Rashba spin-orbit coupling, i.e. $\lambda_R = 0$, the two spin sectors decouple and each of them can be independently modeled by a Haldane Hamiltonian,

$$H = t \sum_{\langle ij \rangle} c_i^\dagger c_j + t_2 \sum_{\langle\langle ij \rangle\rangle} c_i^\dagger c_j + t_3 \sum_{\langle\langle\langle ij \rangle\rangle\rangle} c_i^\dagger c_j + \frac{i\lambda_{SO}}{3\sqrt{3}} \sum_{\langle\langle ij \rangle\rangle} v_{ij} c_i^\dagger c_j + M_S \sum_i \eta_i c_i^\dagger c_i, \quad (2)$$

2b. Topological invariants

The usual characterization of two-dimensional topological systems is done in terms of (spin) Chern numbers. However, as a two-dimensional system gets thinner, it can be modeled as periodic in the long direction and open in the direction perpendicular to the ribbon. Consequently, the spatial coordinate in the long direction can be Fourier transformed, resulting in a ribbon Hamiltonian. This Hamiltonian only has a single momentum index; the width of the ribbon gives rise to multiple bands instead of the two bulk bands of the usual Haldane model. Since this new ribbon Hamiltonian has a bulk that is parametrized by a single momentum index, its topological characterization is done in terms of a Zak phase. In particular, one must use the multiband Zak phase,

$$\varphi = -\text{Im} \log \det \prod_{j=0}^{N-1} S(k_j, k_{j+1}). \quad (3)$$

Here, $S(k_j, k_{j+1})$ is the overlap matrix of occupied Bloch functions, with elements $S_{mn} \equiv \langle u_{mk_j} | u_{nk_{j+1}} \rangle$. The Bloch eigenfunctions $|u_{nk_j}\rangle$ are obtained numerically by diagonalizing the ribbon Bloch Hamiltonian associated to Eq. (2) at (discretized) momentum $k_j = 2\pi j/(Na)$, with N and a denoting the lattice discretization number and lattice constant, respectively. From the Zak phase, a topological invariant ν is constructed by comparing the Zak phase to the one corresponding to the trivial limit, i.e. $M_s \rightarrow \pm\infty$,

$$\nu \equiv \frac{\varphi - \varphi_{M_s \rightarrow \pm\infty}}{\pi} \text{ mod } 2. \quad (4)$$

Further details regarding the topological invariant ν for nanoribbons is presented in the SM.

2c. LDOS

Although the spectral properties of germanene nanoribbons are not experimentally accessible, the local density of states (LDOS) are promptly accessible by measuring the dI/dV . The LDOS at energy E and position \mathbf{r} can be calculated using

$$\text{LDOS}(E, \mathbf{r}) = \frac{1}{\pi} \sum_n |\psi_n(\mathbf{r})|^2 \frac{b}{(E - E_n)^2 + b^2}, \quad (5)$$

where the wavefunctions $\psi_n(\mathbf{r})$ and the corresponding energies E_n are obtained by numerically diagonalizing Eq. (1). Furthermore, a broadening of $b = 0.05$ eV is incorporated to account for thermal effects and broadening due to lock-in techniques.

References

1. Hasan, M. Z. & Kane, C. L. *Colloquium: Topological insulators. Rev. Mod. Phys.* **82**, 3045–3067 (2010).
2. Kane, C. L. & Mele, E. J. Z_2 Topological Order and the Quantum Spin Hall Effect. *Phys. Rev. Lett.* **95**, 146802 (2005).
3. Kane, C. L. & Mele, E. J. Quantum Spin Hall Effect in Graphene. *Phys. Rev. Lett.* **95**, 226801 (2005).
4. Bernevig, B. A., Hughes, T. L. & Zhang, S.-C. Quantum Spin Hall Effect and Topological Phase Transition in HgTe Quantum Wells. *Science* **314**, 1757–1761 (2006).
5. Kitaev, A. Yu. Unpaired Majorana fermions in quantum wires. *Physics Uspekhi* **44**, 131 (2001).
6. Kempkes, S. N. *et al.* Robust zero-energy modes in an electronic higher-order topological insulator. *Nat Mater* **18**, 1292–1297 (2019).
7. Schindler, F. *et al.* Higher-order topological insulators. *Sci Adv* **4**, (2018).
8. Qi, X.-L. & Zhang, S.-C. Topological insulators and superconductors. *Rev Mod Phys* **83**, 1057–1110 (2011).
9. Beenakker, C. W. J. Search for Majorana Fermions in Superconductors. *Annu Rev Condens Matter Phys* **4**, 113–136 (2013).
10. Jäck, B. *et al.* Observation of a Majorana zero mode in a topologically protected edge channel. *Science (1979)* **364**, 1255–1259 (2019).
11. Alicea, J. New directions in the pursuit of Majorana fermions in solid state systems. *Reports on Progress in Physics* **75**, 076501 (2012).
12. Rizzo, D. J. *et al.* Topological band engineering of graphene nanoribbons. *Nature* **560**, 204–208 (2018).
13. Li, J. *et al.* Topological phase transition in chiral graphene nanoribbons: from edge bands to end states. *Nat Commun* **12**, 5538 (2021).
14. Traverso, S., Sassetti, M. & Traverso Ziani, N. Emerging topological bound states in Haldane model zigzag nanoribbons. *NPJ Quantum Mater* **9**, 9 (2024).
15. Klaassen, D. J. *et al.* Realization of a one-dimensional topological insulator in ultrathin germanene nanoribbons. *Nat Commun* **16**, 2059 (2025).
16. Gilbert, M. J. Topological electronics. *Commun Phys* **4**, 70 (2021).

17. Collins, J. L. *et al.* Electric-field-tuned topological phase transition in ultrathin Na₃Bi. *Nature* **564**, 390–394 (2018).
18. Bampoulis, P. *et al.* Quantum Spin Hall States and Topological Phase Transition in Germanene. *Phys Rev Lett* **130**, 196401 (2023).
19. Qian, X., Liu, J., Fu, L. & Li, J. Quantum spin Hall effect in two-dimensional transition metal dichalcogenides. *Science (1979)* **346**, 1344–1347 (2014).
20. Matthes, L. & Bechstedt, F. Influence of edge and field effects on topological states of germanene nanoribbons from self-consistent calculations. *Phys Rev B* **90**, 165431 (2014).
21. Ezawa, M. Quantized conductance and field-effect topological quantum transistor in silicene nanoribbons. *Appl Phys Lett* **102**, (2013).
22. Cahangirov, S., Topsakal, M., Aktürk, E., Şahin, H. & Ciraci, S. Two- and One-Dimensional Honeycomb Structures of Silicon and Germanium. *Phys Rev Lett* **102**, 236804 (2009).
23. Molle, A. *et al.* Buckled two-dimensional Xene sheets. *Nat Mater* **16**, 163–169 (2017).
24. Reis, F. *et al.* Bismuthene on a SiC substrate: A candidate for a high-temperature quantum spin Hall material. *Science (1979)* **357**, 287–290 (2017).
25. Drummond, N. D., Zólyomi, V. & Fal'ko, V. I. Electrically tunable band gap in silicene. *Phys Rev B* **85**, 075423 (2012).
26. Liu, C.-C., Feng, W. & Yao, Y. Quantum Spin Hall Effect in Silicene and Two-Dimensional Germanium. *Phys Rev Lett* **107**, 076802 (2011).
27. Gröning, O. *et al.* Engineering of robust topological quantum phases in graphene nanoribbons. *Nature* **560**, 209–213 (2018).
28. Borca, B. *et al.* Image potential states of germanene. *2d Mater* **7**, 035021 (2020).
29. Chegel, R. & Behzad, S. Tunable Electronic, Optical, and Thermal Properties of two-dimensional Germanene via an external electric field. *Sci Rep* **10**, 704 (2020).
30. Reich, S., Maultzsch, J., Thomsen, C. & Ordejón, P. Tight-binding description of graphene. *Phys Rev B* **66**, 035412 (2002).

Acknowledgements

L.E., E.D.v.W., H.J.W.Z., and C.M.S. acknowledge the research program “Materials for the Quantum Age” (QuMat) for financial support. This program (registration number 024.005.006) is part of the Gravitation program financed by the Dutch Ministry of Education, Culture and Science (OCW). P.B. acknowledges financial support from the European Research Council (ERC)

under the European Union's Horizon Europe program grant agreement no. 101162852 title Q-EDGE. H.J.W.Z. and D.J.K are supported by NWO Grant OCENW.M20.232.

Author information

Authors and Affiliations

Institute for Theoretical Physics, Utrecht University, Princetonplein 5, Utrecht, 3584 CC, the Netherlands.

Lumen Eek and Cristiane Morais Smith

Physics of Interfaces and Nanomaterials, MESA+ Institute for Nanotechnology, University of Twente, Drienerlolaan 5, Enschede, 7522 NB, the Netherlands.

Esra D. van 't Westende, Dennis Klaassen, Harold Zandvliet, Pantelis Bampoulis

Contributions

LE and EDvW contributed equally to this work. LE performed the theoretical calculations under the supervision of CMS. EDvW and DJK carried out the STM experiments under the supervision of PB and HJWZ. CMS and PB wrote the paper. All authors contributed to the interpretation of the experimental data, development of the theoretical concepts, and review of the manuscript.

Corresponding authors

Correspondence to [Cristiane Morais Smith](#) or [Pantelis Bampoulis](#).

Ethics declarations

Competing interests

The authors declare no competing interests.